Fabrication and biosensing with graphene edges

Gao, J.

Chapter 4

Quantum-capacitive activation of diazonium-functionalized graphene edges for reversible biosensing

Technologies capable of quantitatively detecting various molecules at trace concentrations without the need for external labels or amplification are crucial for early identification of disease biomarkers in medical diagnostics. In this context, label-free field-effect transistor biosensors based on two-dimensional (2D) materials are highly desired for their exceptional sensitivity. However, the instability of non-covalent interface engineering and variations in device performance lead to poor reproducibility, limiting their use in quantitative analysis. To address these challenges, we functionalize only the edges of graphene by protecting its basal plane with a ceramic material and reversibly modifying the edges using diazonium chemistry. Remarkably, the resulting edge-enhanced graphene quantum capacitor (eGQC) exhibits reusability for up to 100 cycles with reproducible working curves. This achievement enables the robust detection of miRNA-21 molecules, a promising biomarker for early cancer diagnosis, at femtomolar concentrations. The sensing response exhibits a standard deviation of only 41% over 100 continuous miRNA detections, significantly outperforming current state-of-the-art graphene biosensor arrays.

Keywords: Graphene biosensors; edge chemistry; quantum capacitance.

This chapter was published as an article: Jianwei Gao, Yujia Huang, Lei Bao, Andy Jiao, Yi Li, Shen Ao, Honglei Xue, Xiaofang Kang, Guangya Jiang, Wanshuo Gao, Zhenyu Wang, Xinyu Zhu, Jiatong Liu, Xiaoyan Zhang, Chunlei Wan, Grégory F. Schneider, Wangyang Fu. *Materials Today*, 92, 387-395 (2026).

4.1 Introduction

Two-dimensional (2D) field-effect transistors (FET) biosensors, characterized by their label-free operation, rapid detection and high sensitivity, hold great potential for point-of-care testing (POCT).[1-6] To harvest the surface-exposed electronic processes of atomically thin 2D materials, benign non-covalent functionalization is routinely employed, enabling biomolecular identification at femtomolar (fM) or even sub-fM levels.[6-8] However, the weak van der Waals interaction in non-covalent interface engineering poses an essential challenge for achieving reliable and reproducible sensing.[9-11] In contrast, while covalent functionalization provides robust and reliable attachment,[12,13] they convert the delocalized sp^2 hybridization in graphene to localized sp^3 states, which significantly deteriorates its electrical performance due to Anderson localization.[14,15] This issue is not limited to graphene but also affects other 2D materials with similar bonding and electronic structures. As a result, the achievable density of covalent functionalization is typically hundreds of times lower than monolayer coverage, leading to diminished sensing performance.[16] Compared with covalent functionalization of the basal plane, which disrupts the sp^2 network and degrades electronic performance, edge functionalization preserves the integrity of the basal plane and better maintains device characteristics.[17-19] By confining chemical modification to the edges, sensors can achieve higher sensitivity while minimizing damage to the conductive basal plane relative to widespread basal-plane functionalization.[20-22]Another key challenge in the interface engineering of 2D field-effect biosensors is the restoration of surface cleanliness and chemistry, even after functionalization and reuse.[23-25] While thermal annealing at high temperatures and chemical treatments can partially restore the initial surface state of 2D materials, the harsh conditions required conflict with sensor chip development protocols.[26-28] In addition, the atomic-scale structure of 2D materials like molybdenum disulfide and graphene, renders them vulnerable to damage from CMOS-compatible surface renewal and cleaning technologies, such as plasma ashing.[29,30] Consequently, current 2D field-effect biosensor chips, fabricated through micro/nanofabrication processes, suffer from surface contamination interferences and are typically considered disposable. Although surface regeneration and reusability can be achieved via dissociating the probe from the sensor surface,[31] this approach is significantly limited by the delicate and complex interactions between the sensor surface, sensing probe, and target analyte. These limitations underscore the key importance of advanced interface engineering to fully leverage the capabilities of this sensing platform.

Herein, we show that protecting the basal plane in an edge-enhanced graphene quantum capacitor biosensor chip (eGQC chip) yields reversible covalent functionalization and reusability for up to 100 cycles with reproducible working curves. Recovery of the sensing response at the graphene edges was achieved through oxygen plasma treatment, leaving the basal plane embedded in a ceramic matrix intact. Unlike traditional graphene edge devices—including graphene nanoribbon FETs with a limited edge-to-surface ratio and resist-passivated

devices in which thin dielectric layers reduce but cannot fully suppress the parasitic basal-plane contribution, the ceramic encapsulation employed here physically eliminates basal-plane contact with the electrolyte entirely. This ensures that both the quantum-capacitance signal and the molecular recognition events are confined exclusively to the graphene edges, and crucially, that oxygen plasma regeneration selectively removes biopolymers from the exposed edges without affecting the protected basal plane, enabling robust reusability. By further functionalizing the graphene edges via diazonium chemistry, we successfully track changes in the quantum capacitance of the edges, facilitating quantitative detection of miRNA-21, a potential biomarker for early cancer diagnostics, at dilutions ranging from 10 fM to 10 pM concentrations within several minutes. Remarkably, the standard deviation of calculated relative sensing response $\Delta C/C_0$ over the 100 times continuously miRNA detection concentrated at 41%. Such **e**xcellent reusability of the eGQC-Chip is comparable or even superior to the reported sensing variation of the state-of-the-art Gr-FET array DNA sensor, NH_3 gas sensor, brain activity sensor, and ion sensor ranging from 50% to 178%.[32-35] This detection capability holds great promise for early-stage cancer diagnostics, positioning our approach as a robust foundation for the development of future POCT medical tools for quantitative diagnostics.

4.2 Results and discussion

4.2.1 Preparation of graphene edges

We used an intercalation and pressure sintering method to expose graphene edges while protecting the graphene basal plane within a ceramic matrix (**Figure 1a**).[36,37] As illustrated in **Figure S1**, hexylamine is introduced into graphene oxide (GO) layers via hydrogen bonding to expand the interlayer spacing. Subsequently, the ceramic precursor, tetraethyl silicate (TEOS), is intercalated between GO layers through hydrophobic interactions. Following hydrolysis and calcination, a GO/SiO_2 composite powder is produced, with thin GO sheets encapsulating small ceramic particles. High-temperature sintering, accompanied by a pressure of 40 MPa, facilitates the reduction of GO and the parallel reassembly of reduced GO (rGO) nanolayers into SiO_2 ceramic. The resulting ordered rGO (6 vol%), with lateral dimensions of several microns, are uniformly dispersed within the dense ceramic matrix, establishing conductive pathways.[38] After vertical cutting of the parallel aligned rGO sheets followed by mechanical polishing, **Figure 1a (and Figure S1-2)** illustrates flat surfaces featuring numerous perpendicular rGO edges tightly embedded within the ceramic matrix.

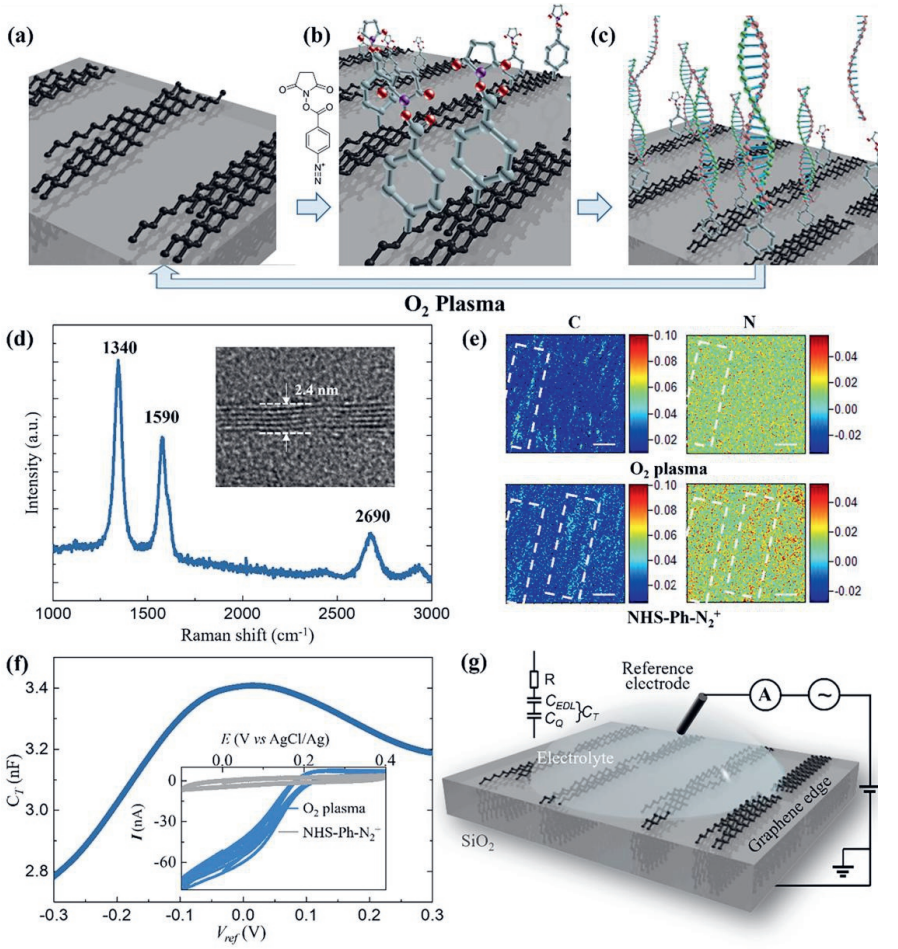

Figure 1. A reusable edge-enhanced graphene quantum capacitor (eGQC) biosensor fabricated by covalent functionalization of graphene edges with diazonium compounds and reset to pristine edges using oxygen plasma treatment. **(a)** Schematic representation of tightly embedded and parallel aligned rGO sheets within the SiO_2 ceramic. **(b)** Graphene edges anchored with NHS-diazonium. **(c)** DNA probes (green) incubated at the graphene edge hybridize with target miRNA. **(d)** Raman spectrum and high-resolution TEM image of the graphene edge. **(e)** TOF-SIMS mapping showing the spatial distribution of C and N elements before and after NHS-diazonium functionalization. Scale bar: 10 μm. **(f)** Total effective interfacial capacitance (C_T) of the eGQC chip plotted against reference voltage (V_{ref}). Inset: Electrochemical activity at the graphene edges probed with $K_3Fe(CN)_6$ before (O_2 plasma, blue) and after 10 cycles (NHS-diazonium grafted, grey) of diazonium chemistry. **(g)** Schematic illustration of the interfacial capacitance measurement.

4.2.2 Functionalization of graphene edges

The exposed pristine edge's quantum capacitance, proportional to the local density of states (DOS), can be leveraged for sensing applications.[36,39] Nevertheless, achieving specific sensing response necessitates the functionalization of the graphene edge. We addressed this challenge by covalently modifying the exposed graphene edges with 4-N-Hydroxy succinimide benzene diazonium tetrafluoroborate salts (NHS-diazonium). Since the base is protected within the ceramic, the sensor's electronic characteristics remain intact, with the sensing response area relying solely on the edge response.

Figure 1b shows the conceptual diagram (see **Figure S3** for more details) of the electrochemical reaction between graphene edge as working electrode and diazonium salt. Aryl radicals were electro-grafted from a 5 mM solution of NHS-diazonium, which undergoes N_2 cleavage and the formation of an electrophilic NHS-aryl radical in relation to the nucleophilic graphene edge.[40,41] The application of a potential difference across the graphene edge and its counter electrode not only induces electrophilic reactions, but also enhances the energy levels of the electron density of states of graphene edge, overlapping its HOMO with the LUMO of the aryl radicals and facilitating its binding to the carbon atoms as well as potential hydroxyl and carboxyl groups at the graphene edge.[17,40] Subsequently, the NHS groups on the grafted diazonium salt are further incubated with amino-modified DNA to enable highly selective detection of biomarkers (**Figure 1c**). The introduction of varying concentrations of target miRNA results in miRNA/DNA hybridization at the edge of graphene, inducing a noticeable change in quantum capacitance.[36,42] Upon completion of the test, the sensing area can be effectively restored through oxygen plasma treatment, without affecting the basal plane that is protected by the ceramic matrix (**Figure 1a-c**).

Figure 1d gives the Raman spectroscopy analysis on the oxygen plasma treated rGO/SiO_2 composite, where the characteristic 2D band ($\approx$2690 cm^{-1}), G band ($\approx$1590 cm^{-1}), and the defect-related D band ($\approx$1340 cm^{-1}) of graphene could be clearly identified.[43,44] The average thickness and interlayer spacing of the rGO sheets can be identified as seven layers on average and 0.35 nm, respectively (the inset of **Figure 1d**). **Figure 1f (inset)** compares the cyclic voltammetry (CV) cycles in the presence of 5 mM $K_3Fe(CN)_6$ in 0.1 M KCl conducted before (blue) and after (grey) the electro-grafting of the NHS-aryl radicals. The formation of an insulating NHS passivation layer results in the suppression of electron exchange with the redox-probe in the electrolyte, as evidenced by the decrease in the intensity of the redox current, as well as the increased Raman intensity ratio I_D/I_G (**Figure S4**). Notably, during continuous CV cycles, the CV curves stabilized after the initial two cycles, which can be attributed to the formation of an insulating NHS layer that passivates the graphene edges, effectively preventing further binding of NHS-aryl radicals.[40,45] (**Figure S5**)

One step further, we employed Low-Energy Ion Scattering (LEIS) and Secondary Ion Mass

Spectrometry (SIMS) to characterize the graphene edge device before and after electro-grafting of NHS-diazonium (**Figure S6 and S7**). In agreement with previous findings, LEIS showed the expected spectral features, confirmed by the appearance of the nitrogen (N) element signal at an energy of 1027 eV, as well as by the carbon (C) element at 848 eV (**Figure S6**). Furthermore, the electro-grafting of the NHS-diazonium onto the graphene edge was verified by the appearance of a SMIS-peak at 14.1 m/z, corresponding to N element. Remarkably, spatial-resolved analysis of C and N elements revealed the distribution of the C from the graphene edge across the sample surface, with no discernable N signal, as expected after oxygen plasma treatment (**Figure 1e**). After electrochemical grafting of NHS-diazonium, N element from the diazonium compounds can be observed with a distribution aligning closely with that of the C element (**Figure 1e**), indicating successful functionalization. Notably, regenerating the diazonium covalent functionalization confirms that the N distribution still closely matched that of the C atoms (**Figure S7b**). Clearly, the reversible covalently functionalization retains a consistent element distribution, and the robust edge chemistry ensures the reliability and repeatability of the sensor's performance.

4.2.3 Electrical characterization of the eGQC chip

We employed a two-terminal configuration and previously reported Constant-Phase-Element (CPE) parameters (*m*, which reflect the degree of inhomogeneity in the graphene edge morphology and distribution)[46] to quantify the total effective interfacial capacitance (C_T) of the graphene edges. This capacitance includes both the quantum capacitance (C_Q) and the electrical double-layer capacitance (C_{EDL}) in series (**Figure 1g**). To regulate electrostatic potential, a 100 mV sine wave was superimposed on a direct current (DC) bias voltage applied to a reference electrode immersed in an electrolyte solution. Notably, a liquid seal made from biocompatible and insulating silicon rubber was applied to minimized potential leakage current and parasitic capacitance, by preventing any potential exposure of the graphene edges and metal electrodes to the electrolyte, aside from an opening window with a diameter (d) of 0.6 mm, resulting in an effective area $S_{eff}=\pi d^2/4\approx0.3$ mm^2.

We monitored the bias-dependent effective interfacial capacitance (C_T) at an intermediate frequency of 172 Hz, where the capacitive impedance is dominant and stable with frequency, to strike a balance between electrical noise at low frequencies and reduced accuracy at high frequencies due to decreasing capacitive reactance (see also **Figure S8** for frequency-dependent current and phase measured in a 0.01×PBS solution). **Figure 1f** shows the C_T as a function of V_{ref}, ranging from -0.3 V to +0.3 V. The capacitance curve exhibits an unusual 'Λ'-shaped profile, peaking near V_{ref}=0 V. By normalizing C_T to the effective area, the quantum capacitance C_Q of graphene edges can be determined based on the series capacitance model: $C_Q= C_{EDL}C_T/(C_{EDL}-C_T)$, where the electric double-layer capacitance C_{EDL} is assumed constant, given its minimal variation against electrolyte gating over the relatively small voltage range (±0.3 V).[36,47] Notably,

the Gouy-Chapman (GC) model is also applied to account for C_{EDL} at improved accuracy. No significant deviation in the resulting C_Q behavior was observed, which retains a similar 'Λ'-shaped profile (see also **Figure 2b**). We also measured quantum-capacitance from three eGQC devices produced in independent fabrication batches (**Figure S9**). These three-device $C_T - V_{ref}$ curves consistently exhibit the characteristic 'Λ' shape observed in the main text. While there are minor shifts in peak position and amplitude between devices (attributable to routine fabrication tolerances such as slice polishing, local rGO density and contact placement), the C_T values remain the same order of magnitude across devices, demonstrating reproducible edge-specific behavior. We evaluated surface morphology before and after diazonium electro-grafting using SEM. SEM images of the exposed edge region acquired pre- and post-grafting show no detectable change in edge topography at the SEM resolution employed (no particulate deposition or gross restructuring was observed in **Figure S10**).

AFM and STM are both powerful tools for atomic morphology characterization, unfortunately, they are not applicable to our samples due to intrinsic roughness of the ceramic-embedded graphene structure. It should be emphasized that the design of our device inherently restricts the reaction to the graphene edges. During fabrication, graphene sheets are fully encapsulated within a dense SiO_2 matrix by pressure sintering, leaving only their edges accessible after oxygen plasma etching (**Fig. 1d** inset). The O_2 plasma treatment removes any exposed basal plane carbon, ensuring that only the edge sites remain exposed to the electrolyte. Furthermore, independent surface/electrochemical probes confirm graphene edge modification: 1) $K_3Fe(CN)_6$ cyclic voltammetry shows suppressed/stabilized redox peaks (**Fig. 1f**, insulating edge passivation layer); 2) repeated O_2 plasma regeneration yields reproducible C_T/C_Q behavior (**Fig. 1f**, **2c**, **3a-b**), only achievable if functionalization/regeneration are confined to exposed edges (not variable basal-plane coverage) 3) Moreover, we note that oxygen plasma etching under our processing conditions does not attack the SiO_2 ceramic. As shown in **Figure S11**, SEM characterization of the ceramic surface before and after O_2 plasma treatment exhibits no measurable change in morphology, confirming that the ceramic matrix remains intact under the plasma conditions used. Because the graphene basal planes are embedded and sealed within this dense SiO_2 matrix, they are not exposed to the electrolyte, to O_2 plasma, or to the electrochemical environment during diazonium grafting. Moreover, electrochemical diazonium grafting requires an electrically conductive, electrolyte-accessible surface to drive radical formation and covalent attachment; in our devices the only such regions are the exposed graphene edges.

To shed light on the quantum capacitance behavior of graphene edges, we conducted density functional theory (DFT) simulations to evaluate the localized density of states near the Fermi energy for pristine graphene edges in a zigzag configuration (black line), with additional hydroxyl (-OH) groups (green line), and with grafted -Ph-NHS groups (red line), as illustrated in **Figure 2a**. The disrupted symmetry at the edges leads to discontinuities and unfilled p_z

orbitals in the outermost carbon atoms, creating high-energy quasi-localized states near the Fermi level. Consequently, the calculated C_Q curve in **Figure 2b** displays a ' ∧ '-shaped profile, reflecting this phenomenon and matching with our experimental results (dash line). Following oxygen plasma ashing, the incorporation of oxygen-containing groups (for instance, hydroxyl groups simulated here) at the graphene edges increases the density of states due to oxygen atom doping, which enhances the quantum capacitance. After NHS-diazonium modification, the electron-withdrawing effect of the diazonium groups shifts the Fermi energy slightly to the left (**Figure 2b**), aligning with our experimental results presented in **Figure 2c**.

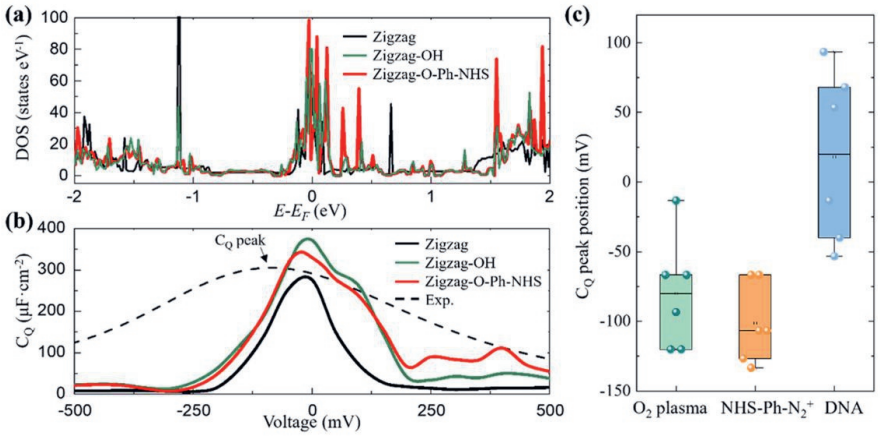

Figure 2. Calculated DOS and quantum capacitance of the eGQC chip. (a) The calculated DOS of a graphene edge in zigzag configuration (black line), with hydroxyl (-OH) groups (green line), and with grafted -Ph-NHS groups (red line), and the calculated quantum capacitance **(b),** respectively. The dashed line represents the experimental results. **c)** The shift of the peak position of the $C_Q\,(V_{ref})$ curves under different functionalization stages.

After successful branching NHS-diazonium through electrochemical grafting, we proceeded to immobilize 5'-amino-modified DNA probe molecules onto the graphene edges by reacting the active eater of NHS with the amino groups by incubation at room temperature for 4 hours. Following the completion of the incubation, the device was thoroughly rinsed with deionized water to remove any weakly bound DNA molecules, ensuring only covalently attached probes remained on the edges. The attachment of negatively charged DNA molecules at the graphene edges is confirmed by the significant positive shift of the peak position of the $C_Q\,(V_{ref})$ curves (**Figure 2c,** see also **Figure S12**).

4.2.4 Renewable sensing at the edge of graphene

After immobilizing DNA probes at the graphene edge, we incubated the sensor with 0.05% Tween-20 for 30 minutes to prevent non-specific adsorption, proceeded with the testing of target miRNA at varying concentrations. As shown in **Figure 3a**, the addition of 10 fM miRNA led to a significant decrease in capacitance during real-time measurements of the eGQC chip

(see also **Figure S13**). As the target miRNA concentration increased to 100 fM, 1 pM and 10 pM, the capacitance gradually decreased due to the doping effect from charge accumulation. Following the sensing tests, the eGQC chip was reinitialized using O_2 plasma etching treatment (90 W/120 s with a graphene etching rate of 4.4 nm/min, **Figure S14**), which effectively removes biopolymers at the graphene edges (**Figure S12**). To test the sensor's reusability, this regeneration process was repeated 100 times on the same device and no significant degradation in both the capacitance profiles (**Figure S12b**) and sensor's response to the miRNA was observed during the 100 consecutive tests (**Figure 3b**).

The etching treatment effectively restores the graphene edge to its original state as verified by the relatively narrow variations in the relative total effective interfacial capacitance (**Figure S15**), which can be fit with a normal distribution with a peak of 18 ± 1.9%. Remarkably, the standard deviation of calculated relative sensing response $\Delta C/C_0$ over the 100 times continuously miRNA detection concentrated at 41% (**Figure 3c** and **Figure S16**). Such excellent reusability of the eGQC-Chip is comparable or even superior to the reported sensing standard deviation of the state-of-the-art Gr-FET array DNA sensor,[35] NH_3 gas sensor,[32] brain activity sensor,[33] and ion sensor[34] ranging from 50% to 178% (**Figure 3d)**. We also performed a normal distribution fitting of the experimental results, showing that our sensor exhibits a normal distribution range of 8.9 ± 1.7%, whereas the reported sensors in the state-of-the-art non-covalent functionalized Gr-FET array demonstrate normal distribution ranges from 16 ± 3.8% to 56 ± 4.4% (Figure S**16)**. Furthermore, compared to existing covalently functionalized Gr-FET biosensors,[9,48-50] the eGQC-Chip shows a significantly enhanced detection limit by at least two orders of magnitude to achieve femtomolar levels (**Figure 3e and Table S1**), by allowing the sensing response to rely solely on the graphene edges and ensuring the effective molecular binding while preserving its electronic properties. In comparison, due to Anderson localization upon the transition of sp^2 to sp^3 hybridization during covalent functionalization, the density of functionalization is fundamentally limited and accompanied with significant degradation in the electrical performance (**Figure S17** and **S18**).

Figure 3f demonstrates the selectivity of the sensor chip, tested against non-complementary RNA sequences (see also **Figure S19**). The introduction of fully complementary miRNA resulted in a substantial and distinct modulation of the sensing response, reflecting its higher binding affinity compared to the non-complementary miRNA sequences at minimal response. Single-base mismatch discrimination was evaluated (**Figure S19**) by testing single-base ‑ mismatched miRNA sequences alongside fully complementary and non-complementary controls. The eGQC sensor yields an intermediate capacitance response for single-base mismatches relative to fully complementary and non-complementary targets, consistent with the reduced hybridization free energy of mismatched duplexes and demonstrating sensitivity to small changes in probe ‑ target binding thermodynamics. In another control measurement, we tested the sensing response of graphene edges untreated or passivated with Tween-20. The

negligible sensing responses (less than 10% compared to those of the untreated graphene edges, **Figure S20**), unambiguously confirms the effectiveness of Tween-20 in preventing nonspecific adsorption.

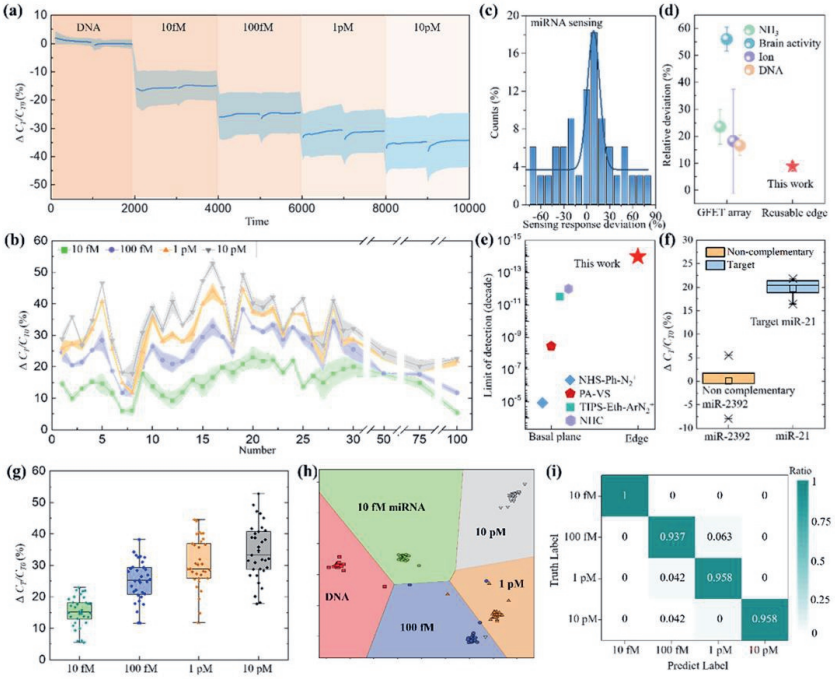

Figure 3. Renewable sensing at the graphene edge. (a) Capacitance response of the eGQC chip during the detection of miRNA at concentrations of 10 fM, 100 fM, 1 pM, and 10 pM. After each measurement, the device was regenerated using O_2 plasma ashing (90 W, 120 s) and tested repeatedly for 100 cycles. **(b)** Capacitance responses for miRNA concentrations of 10 fM, 100 fM, 1 pM, and 10 pM over 100 consecutive regeneration and measurement cycles. **(c)** Relative deviation of the eGQC sensor's capacitance response for 10 pM miRNA detection across 100 consecutive tests. **(d)** Comparison of sensing response fluctuations for regenerated eGQC during continuous measurements among the state-of-the-art Gr-FET arrays, including DNA, NH_3, brain activity, and ion sensor. **(e)** Detection limit comparison of the current covalently functionalized graphene biosensor, including NHS-diazonium, vinylsulfonated-polyamines (PA-VS), TIPS-Eth-ArN_2^+, and N-Heterocyclic Carbene (NHC). **(f)** Selectivity performance of the eGQC device. **(g)** Statistical analysis of capacitance response to miRNA at different concentrations over 100 tests. **(h)** LDA analysis for eGQC device in solutions with varying miRNA concentrations. **(i)** Confusion matrix of the multi-output classification model for different miRNA concentration levels.

Figure 3g shows the statistical analysis of the capacitance responses at various miRNA concentrations over repeated tests, which increases rapidly with rising miRNA concentrations before gradually approaching saturation. The heat map of capacitance responses across 100 repeated tests (**Figure S21**) also displays a consistent and measurable increasing capacitance

response across multiple test iterations.

Despite the promising results from repeated tests, some overlap in detection signals for target molecules was observed, particularly at higher concentration (10 pM, **Figure 3g**), as also indicated by the overlapping colors in the heat map in **Figure S21**. This overlap suggests difficulty in distinguishing between target molecule concentrations at saturation levels. To improve sensing accuracy, we applied machine learning algorithms. **Figure 3h** demonstrates the use of linear discriminant analysis to project multivariate data into a lower-dimensional space while preserving maximum variance. The distinct separation of clusters representing different miRNA concentrations highlights the sensor's ability to differentiate between various concentrations in solution. To further reduce signal overlap and ensure reliable detection, we employed an LDA classifier, as shown in **Figure 3i**, which achieved prediction accuracies of 93.7–100% after training. The clear capacitance response to miRNA at femtomolar (fM) concentrations demonstrates the impressive detection capabilities of the eGQC-Chip, maintaining distinct signal differences across the full concentration range (10 fM–10 pM) even after 100 consecutive tests. Assuming a linear response at low concentrations, the limit of detection (LOD) can be estimated to be 147 aM, corresponding to a signal-to-noise ratio (SNR) of 3. These results surpass those of conventional ELISA measurements[51] and are comparable to cutting-edge Single Molecular Array (Simoa) biosensing technology[52], but with more streamlined workflow shorter testing time, positioning the eGQC sensor as a valuable tool for earlier disease diagnosis across a range of medical applications.

4.2.5 Fringe enhancement of electric fields at the graphene edges

Biosensors typically detect biomarkers by binding target molecules to probe molecules immobilized on the sensor surface. This process is often hindered by diffusion kinetics, where the binding efficiency is limited by thermodynamic diffusion, therefore resulting in slowing down the response time of the sensor particularly at low concentrations. To address this problem, we leverage the sharp edges of graphene to facilitate the generation of strong electrostatic fields (**Figure 4a**), as validated using COMSOL Multiphysics® simulations. **Figure 4b** shows the local electrical field distribution during the operation of the eGQC detector with a +0.8 V potential voltage applied to the graphene edge with the electrolyte solution grounded. A steep voltage drop near the graphene edge leads to significant fringe enhancement of the local electric field, which is 10 times stronger than just 1 nm away (**Figure 4b**) and actively attracts and concentrates charged target molecules for efficient and robust biomolecular detection. Direct optical visualization of biomolecule enrichment near the graphene edges was not feasible because fluorophores positioned within a few nanometres of graphene experience strong near-field quenching, which drastically suppresses their fluorescence emission.[53,54] This intrinsic quenching effect makes single-molecule fluorescence tracking unreliable for quantitatively assessing molecular accumulation at the edge interface.Furthermore, we incubated both

negative (repulsive) and positive (attractive) biased eGQC-Chips in DNA solution (negatively charged), followed by conducting elemental analysis using X-ray photoelectron spectroscopy (XPS). As shown in **Figure 4c-d**, the fact that the intensity of the N1s and P2p peaks increased significantly under the positive biased condition compared to the negative one, clearly suggests a controllable DNA enrichment by fringe enhancement of electric fields at the graphene edges. This supports our ability to rapidly detect miRNA at concentrations as low as fM, and even sub-fM levels.

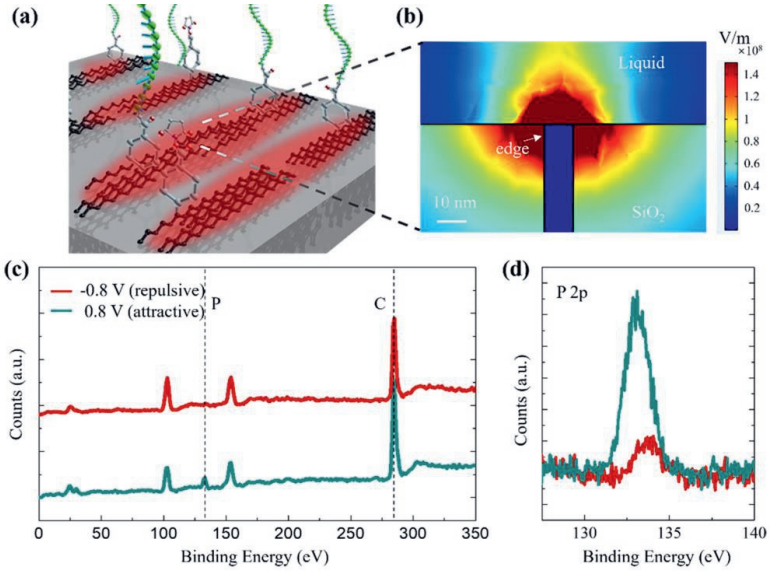

Figure 4. **Fringe enhancement of electric fields at the graphene edges. (a)** Schematic illustration of the local electric field distribution at the graphene edge. **(b)** COMSOL simulation results depicting the electrostatic field at graphene edges. **(c)** XPS analysis showing elemental composition of DNA located at the edge of graphene under both positive (attractive) and negative (repulsive) biased conditions. **(d)** P elements analysis.

4.3 Conclusion

We present a covalent functionalization of eGQC-Chip by protecting the basal surface of graphene using ceramics. Employing diazonium covalent functionalization at the edges ensures the effectiveness of molecular binding without compromising the electronic properties of the sensor. By effectively removing the molecules residing at the graphene edges through oxygen plasma treatment, the graphene edges can be reset to pristine, and the eGQC-Chip can be reused over hundred times without performance loss. Therefore, this novel approach overcomes the limitations of traditional covalent modifications and can be adapted to other 2D materials, paving the way for alternative sensing technologies involving graphene edges. While individual devices demonstrate excellent reusability over 100 cycles, the multi-step fabrication process, which involving GO intercalation, hydrolysis, and sintering, introduces variability between

devices, and the resulting inter-device inconsistency remains relatively large compared to conventional microfabricated sensors.

4.4 Methods

Device fabrication

The rGO/SiO_2 bulk was synthesized using an intercalation and pressure sintering method as previously described. [14,15] Graphene oxide (GO), which contains oxygen-functional groups, was first manually ground and then reacted with hydroxyapatite (HA). Tetraethyl orthosilicate (TEOS) was subsequently co-intercalated into the GO structure by stirring at 40°C for 4 hours. After hydrolysis and heat treatment at 400°C for 2 hours under a nitrogen atmosphere, the GO/SiO_2 powder was obtained. The powder was then densified into rGO/SiO_2 ceramic bulk using spark plasma sintering at 1350°C and 40 MPa under vacuum. The bulk material was processed into thin slices (~150 μm thick) by cutting perpendicular to the aligned rGO sheets with a diamond wire saw. To remove adsorbed impurities, the slices were further polished and etched using oxygen plasma. The SiO_2 ceramic matrix acts as a mechanically robust, electrically insulating, and chemically stable scaffold, while rGO domains form localized conductive networks confined within the SiO_2 framework. Different from general deposition method, graphene sheets and SiO_2 matrix are closely integrated through ceramic synthesis method. This structural confinement physically protects the graphene edges from environmental degradation and simultaneously enables the isolation of edge-localized quantum-capacitance signals from parasitic background effects. The etched slices were integrated into the external circuit by connecting them to copper wires. Each slice was mounted in a small plastic housing, secured with non-toxic, self-curing rubber. The housing was equipped with a saturated Ag/AgCl reference electrode and two liquid injection ports and sealed with a glass slide. The nano-laminated rGO/SiO_2 was attached to a silver electrode, with the interface encapsulated in insulating silicone rubber. A sensing window approximately 0.6 mm in diameter was created to expose the functionalized rGO/SiO_2 while isolating the silver electrode from the electrolyte. This design minimizes potential leakage currents and parasitic capacitance, ensuring precise and stable measurements with the eGQC-Chip.

Computational methods

Theoretical capacitance was computed using the Vienna Ab Initio Simulation Package (VASP) through Density Functional Theory (DFT) calculations.[55,56] The generalized gradient approximation employing the Perdew–Burke–Ernzerhof functional (GGA-PBE) was employed to describe the exchange correlations of the electron interactions. The Van der Waals dispersion corrections were implemented using the optB86b-vdW functional.[57,58] The ionic cores were described by the projector augmented-wave (PAW) pseudopotentials with an energy cutoff of 520 eV. The energy and force convergence criteria were set to 10^{-4} eV and 0.02 eV $Å^{-1}$,

respectively. A seven-layered graphene zigzag edge model[36] (**Figure S22**) was created and passivated by hydroxyl groups or hydrogen atoms. A periodic boundary condition was set in the *z* direction, and vacuum slabs were added in the *x* and *y* directions. The atoms below the green rectangle were fixed to mimic the bulk graphene, while atoms above the green rectangle were allowed to relax to mimic the edge. The final dimensions of the model were 34.84 Å × 35.05 Å × 17.27 Å. A (3×3×6) Monkhorst-Pack k-mesh was sampled for the calculation of DOS. Spin polarization of zigzag edges was beyond the scope of our model, as it is only meaningful for narrow graphene nanoribbons.[59] We note that our DFT modeling omitted explicit spin polarization. Spin-polarized edge magnetism is most pronounced for ideal, narrow zig-zag nanoribbons in vacuum; by contrast, our devices comprise micrometer-scale, multilayer rGO sheets whose edges are chemically modified (oxygen-containing terminations after plasma and covalent diazonium branches) and are embedded in a high-dielectric SiO_2 matrix and measured in an electrolyte. Interlayer coupling, chemical passivation and dielectric/electrolyte screening are all expected to quench or strongly perturb the magnetic ordering found in ideal ribbons, so spin polarization is unlikely to control the large-scale C_Q behaviour observed here. In practice, non-spin DFT calculations reproduce the key experimental feature: a '∧'-shaped C_Q–V_{ref} curve produced by high-energy, quasi-localized p_z states at the graphene edges. These calculations also capture the qualitative shifts of the curve caused by oxidation and by grafting of electron-withdrawing diazonium groups. While spin polarization would modify fine spectral details (for example, very low-energy splittings), it would not eliminate the enhanced density of states near the Fermi level that produces the ∧-shape; therefore the principal interpretation and conclusions of this work is still valid even if explicit spin effects are omitted. Electrolyte screening was considered in our analysis because it directly couples to the measured interfacial capacitance. All C_Q measurements were acquired in the 0.01×PBS, so solvent and ion screening are inherently sampled by the experiments. For 0.01×PBS the Debye screening length is on the order of 10 nm, which is comparable to the probe-target complex. Consequently, target molecules captured at the graphene edge remain well within the screening length and thus perturb the quantum capacitance. Previous experimental and theoretical studies have shown that the interaction of water molecules with graphene exerts only a secondary influence on its adsorption behavior and electronic structure.[36,60,61] This weak perturbation arises from the low adsorption energy of H_2O on graphene (typically <0.2 eV),[62] implying minimal modification of the electronic density of states near the Fermi level. In addition, our earlier work[36] demonstrated that electrolytes such as KCl exhibit limited specific adsorption at graphene edges, as both K^+ and Cl^- ions are chemically inert and show little affinity for direct binding to the carbon lattice.

Electrical measurements

Based on the equivalent circuit model (**Figure 1g**) and parameters from the constant phase element (CPE) model, the impedance Z is defined as:

$$Z = R + Z_{CPE} = R + (K(i\omega)^m)^{-1} \quad (1)$$

Where R is the resistance, K is the differential capacitance at the interface when $m = 1$, $i = (-1)^{0.5}$ is the imaginary unit, $\omega = 2\pi f$ is the angular velocity of the applied alternating voltage V, and m is the fractional exponent parameter of CPE. The effective capacitance C_T can therefore be expressed as,

$$C_T = K^{1/m} R^{(1-m)/m} \quad (2)$$

$$1/C_T = 1/C_Q + 1/C_{EDL} \quad (3)$$

Where C_Q is the quantum capacitance, and C_{EDL} is the electric double-layer capacitance. Using Equations (1) and (2), v we measured the current-voltage I-V_{ref} relationship at the operational frequency, enabling conversion to the C_T-V_{ref} curve. Additionally, at a fixed V_{ref}, the current-time (I-t) curve was recorded, from which the resistance-time (R-t) and capacitance-time (C_T-t) curves were derived. All experiments were performed using at least three independently fabricated devices unless otherwise stated. Data are presented as mean ± standard deviation (SD). Error bars in figures represent one standard deviation from the mean. Linear regression was used to determine sensor sensitivity from the slope of the calibration curves. The goodness of fit was evaluated using the coefficient of determination (R^2). The limit of detection (LOD) was calculated as $3\sigma/S$, where σ is the standard deviation of the blank signal and S is the slope of the calibration curve. Ninety-five percent confidence intervals (95% CI) were calculated for all fitted sensitivity values

Relative deviation calculation

The relative deviation of the eGQC sensing response was calculated as the absolute difference between an effective capacitance sensing response (ΔC_T), where ΔC_T represents the difference between the effective capacitance (C_T) after sensing and the initial capacitance (C_T) following DNA functionalization, and the mean effective capacitance sensing response ($\overline{\Delta C_T}$) across multiple repeats. This value was then normalized by the mean effective capacitance sensing response using the formula: $\frac{\Delta C_T - \overline{\Delta C_T}}{\overline{\Delta C_T}}$. The relative sensing response was evaluated over 100 consecutive miRNA detections at a concentration of 10 pM. For comparison, the performance of non-covalently functionalized Gr-FET arrays was examined by analyzing either the deviation in Dirac point positions or the relative source-drain current deviation. The Dirac point deviation was calculated as the absolute difference between an individual device's Dirac point (V_{Dirac}) and the array's mean Dirac point ($\overline{V_{Dirac}}$), normalized by the array's mean Dirac point: $\frac{V_{Dirac} - \overline{V_{Dirac}}}{\overline{V_{Dirac}}}$, or the relative source-drain current deviation, calculated as the absolute difference between a single device's response and the array's mean response, normalized by the array's mean response, $\frac{I_{ds} - \overline{I_{ds}}}{\overline{I_{ds}}}$. Following the calculation of the normalized signal response, the

data were statistically analyzed within predefined intervals to determine the frequency of devices within each signal response range. The count of devices in each interval was then divided by the total number of devices to determine the percentage of devices within each range. A normal distribution fitting was subsequently performed on the percentage data to obtain the mean (corresponding to the position of the peak) and the standard deviation.

Synthesis of NHS-diazonium (same procedure as described in chapter 2)

A 250 ml round bottom flask was charged with 4-aminobenzoic acid (1.4 g, 10 mmol), EDC (3.1 g, 20 mmol) and N-Hydroxy succinimide (1.8 g, 15 mmol). CH_2Cl_2 (100 ml) was added and the suspension was stirred at room temperature for 3 h. Then, H_2O (50 ml) was added and the layers were separated. The organic layer was washed with H_2O (2 × 50 ml), brine (1 × 50 ml), and dried over $MgSO_4$. The mixture was concentrated under reduced pressure to yield NHS-aniline as a white fluffy solid (1.8 g, 7.7 mmol). NHS-aniline (1.8 g, 7.7 mmol) was suspended in HBF_4 (48 wt. % in H_2O, 10 ml) to obtain a white suspension. After cooling on ice, $NaNO_2$ (0.56 g, 8.1 mmol) in H_2O was slowly added dropwise over 30 min to obtain a yellow suspension, and the reaction mixture was stirred while slowly warming up to RT for 30 min. Then, the mixture was cooled on ice, filtered over a glass frit and washed with ice-cold water (30 ml), methanol (20 ml) and diethylether (30 ml). This residue was dried over air, and then in vacuo to obtain a faint yellow solid (1.9 g, 5.6 mmol, 56% over two steps). ^{1}H NMR (600 MHz, DMSO-d_6) δ 8.90 (d, J = 8.8 Hz, 1H), 8.62 (d, J = 8.9 Hz, 1H), 2.93 (s, 2H). ^{13}C NMR (151 MHz, DMSO-d_6) δ 169.92, 159.88, 133.75, 133.54, 132.14, 122.65, 25.64, as shown in **Figure S23-28**.

4.5 References

1 Im, H. *et al*. A Dielectric-modulated Field-effect Transistor for Biosensing. *Nature Nanotechnology* **2**, 430-434 (2007). https://doi.org/10.1038/nnano.2007.180

2 Zhang, X. *et al.* Dielectric-modulated Biosensing with Ultrahigh-frequency-operated Graphene Field-effect Transistors. *Advanced Materials* **34**, 2106666 (2022). https://doi.org/https://doi.org/10.1002/adma.202106666

3 Rodrigo, D. *et al.* Mid-infrared Plasmonic Biosensing with Graphene. *Science* **349**, 165-168 (2015). https://doi.org/10.1126/science.aab2051

4 Rohaizad, N. *et al*. Two-dimensional Materials in Biomedical, Biosensing and Sensing Applications. *Chemical Society Reviews* **50**, 619-657 (2021). https://doi.org/10.1039/D0CS00150C

5 Hajian, R. *et al.* Detection of Unamplified Target Genes via CRISPR–Cas9 Immobilized on a Graphene Field-effect Transistor. *Nature Biomedical Engineering* **3**, 427-437 (2019). https://doi.org/10.1038/s41551-019-0371-x

6 Wang, L. *et al.* Rapid and Ultrasensitive Electromechanical Detection of Ions, Biomolecules and SARS-CoV-2 RNA in Unamplified Samples. *Nature Biomedical Engineering* **6**, 276-285 (2022). https://doi.org/10.1038/s41551-021-00833-7

7 Hwang, M. T. *et al.* Ultrasensitive Detection of Nucleic acids Using Deformed Graphene Channel Field Effect Biosensors. *Nature Communications* **11**, 1543 (2020). https://doi.org/10.1038/s41467-020-15330-9

8 Seo, G. *et al.* Rapid Detection of COVID-19 Causative Virus (SARS-CoV-2) in Human Nasopharyngeal Swab Specimens Using Field-effect Transistor-based Biosensor. *ACS Nano* **14**, 5135-5142 (2020). https://doi.org/10.1021/acsnano.0c02823

9 Kim, K. H. *et al.* N-Heterocyclic Carbene–graphene Nanotransistor Based on Covalent Bond for Ultrastable Biosensors. *Advanced Functional Materials* **34**, 2310377 (2024). https://doi.org/https://doi.org/10.1002/adfm.202310377

10 Kim, K. H. *et al.* Open-bandgap Graphene-based Field-effect Transistor Using Oligo(phenylene-ethynylene) Interfacial Chemistry. *Angewandte Chemie International Editions* **61**, e202209726 (2022). https://doi.org/https://doi.org/10.1002/anie.202209726

11 Fu, W. *et al*. Sensing at the Surface of Graphene Field-effect Transistors. *Advanced Materials* **29**, 1603610 (2017). https://doi.org/https://doi.org/10.1002/adma.201603610

12 Kuila, T. *et al.* Chemical Functionalization of Graphene and Its Applications. *Progress in Materials Science* **57**, 1061-1105 (2012). https://doi.org/https://doi.org/10.1016/j.pmatsci.2012.03.002

13 Georgakilas, V. *et al.* Functionalization of Graphene: Covalent and Non-covalent Approaches, Derivatives and Applications. *Chemical Reviews* **112**, 6156-6214 (2012). https://doi.org/10.1021/cr3000412

14 Leconte, N. *et al.* Quantum Transport in Chemically Modified Two-dimensional Graphene: From Minimal Conductivity to Anderson Localization. *Physical Review B* **84**, 235420 (2011). https://doi.org/10.1103/PhysRevB.84.235420

15 Ćirić, L. *et al.* Defects and Localization in Chemically-derived Graphene. *Physical Review B* **86**, 195139 (2012). https://doi.org/10.1103/PhysRevB.86.195139

16 Johns, J. E. & Hersam, M. C. Atomic Covalent Functionalization of Graphene. *Accounts of Chemical Research* **46**, 77-86 (2013). https://doi.org/10.1021/ar300143e

17 Paulus, G. L. C., Wang, Q. H. & Strano, M. S. Covalent Electron Transfer Chemistry of Graphene with Diazonium Salts. *Accounts of Chemical Research* **46**, 160-170 (2013). https://doi.org/10.1021/ar300119z

18 Sinitskii, A. *et al.* Kinetics of Diazonium Functionalization of Chemically Converted Graphene Nanoribbons. *ACS Nano* **4**, 1949-1954 (2010). https://doi.org/10.1021/nn901899j

19 Sarkar, S. *et al.* Organometallic Hexahapto Functionalization of Single Layer Graphene as a Route to High Mobility Graphene Devices. *Advanced Materials* **25**, 1131-1136 (2013). https://doi.org/https://doi.org/10.1002/adma.201203161

20 Cho, K. M. *et al.* Edge-functionalized Graphene Nanoribbon Chemical Sensor: Comparison with Carbon Nanotube and Graphene. *ACS Applied Materials & Interfaces* **10**, 42905-42914 (2018). https://doi.org/10.1021/acsami.8b16688

21 Neubert, T. J., Krieg, J., Yadav, A. & Balasubramanian, K. pH Sensitivity of Edge-gated Graphene Field-effect Devices with Covalent Edge Functionalization. *ACS Applied Electronic Materials* **4**, 4668-4676 (2022). https://doi.org/10.1021/acsaelm.2c00880

22 Kwon, S. S. *et al.* Reversible and Irreversible Responses of Defect-Engineered Graphene-based Electrolyte-gated pH Sensors. *ACS Applied Materials & Interfaces* **8**, 834-839 (2016). https://doi.org/10.1021/acsami.5b10183

23 Dai, C., Liu, Y. & Wei, D. Two-Dimensional Field-Effect Transistor Sensors: The Road toward Commercialization. *Chemical Reviews* **122**, 10319-10392 (2022). https://doi.org/10.1021/acs.chemrev.1c00924

24 Mao, S. *et al.* Two-dimensional Nanomaterial-based Field-effect Transistors for Chemical and Biological Sensing. *Chemical Society Reviews* **46**, 6872-6904 (2017). https://doi.org/10.1039/C6CS00827E

25 Tran, T.-T. & Mulchandani, A. Carbon Nanotubes and Graphene Nano Field-effect Transistor-based Biosensors. *Trends in Analytical Chemistry* **79**, 222-232 (2016). https://doi.org/https://doi.org/10.1016/j.trac.2015.12.002

26 Lin, Y.-C. *et al.* Graphene Annealing: How Clean Can It Be? *Nano Letters.* **12**, 414-419 (2012). https://doi.org/10.1021/nl203733r

27 Yuan, G. *et al.* Proton-assisted Growth of Ultra-flat Graphene Films. *Nature* **577**, 204-208 (2020). https://doi.org/10.1038/s41586-019-1870-3

28 Hossain, M. Z. *et al.* Chemically Homogeneous and Thermally Reversible Oxidation of Epitaxial Graphene. *Nature Chemistry.* **4**, 305-309 (2012). https://doi.org/10.1038/nchem.1269

29 Jiang, L. *et al*. Quantum and Electrochemical Interplays in Hydrogenated Graphene. *Nature Communications* **9**, 793 (2018). https://doi.org/10.1038/s41467-018-03026-0

30 Liu, Y. *et al.* Layer-by-layer Thinning of MoS_2 by Plasma. *ACS Nano* **7**, 4202-4209 (2013). https://doi.org/10.1021/nn400644t

31 Jiang, Z. *et al.* A Drug-mediated Organic Electrochemical Transistor for Robustly Reusable Biosensors. *Nature Materials* (2024). https://doi.org/10.1038/s41563-024-01970-5

32 Mackin, C. *et al.* Chemiresistive Graphene Sensors for Ammonia Detection. *ACS Applied Materials & Interfaces* **10**, 16169-16176 (2018). https://doi.org/10.1021/acsami.8b00853

33 Garcia-Cortadella, R. *et al.* Graphene Active Sensor Arrays for Long-term and Wireless Mapping of Wide Frequency Band Epicortical Brain Activity. *Nature Communications* **12**, 211 (2021). https://doi.org/10.1038/s41467-020-20546-w

34 Xue, M. *et al.* Integrated Biosensor Platform Based on Graphene Transistor Arrays for Real-time High-accuracy Ion Sensing. *Nature Communications* **13**, 5064 (2022). https://doi.org/10.1038/s41467-022-32749-4

35 Xu, G. *et al.* Electrophoretic and Field-effect Graphene for All-electrical DNA Array Technology. *Nature Communications* **5**, 4866 (2014). https://doi.org/10.1038/ncomms5866

36 Huang, Y. *et al.* Ultrasensitive Quantum Capacitance Detector at the Edge of Graphene. *Materials Today* **73**, 38-46 (2024). https://doi.org/https://doi.org/10.1016/j.mattod.2023.12.011

37 Huang, Y. *et al.* Edge-rich Reduced Graphene Oxide Embedded in Silica-based Laminated Ceramic Composites for Efficient and Robust Electrocatalytic Hydrogen Evolution. *Small Methods* **5**, 2100621 (2021). https://doi.org/https://doi.org/10.1002/smtd.202100621

38 Huang, Y., Yasuda, K. & Wan, C. Intercalation: Constructing Nanolaminated Reduced Graphene Oxide/Silica Ceramics for Lightweight and Mechanically Reliable Electromagnetic Interference Shielding Applications. *ACS Applied Materials & Interfaces* **12**, 55148-55156 (2020). https://doi.org/10.1021/acsami.0c15193

39 Dröscher, S. *et al.* Quantum Capacitance and Density of States of Graphene. *Applied Physics Letters* **96**, 152104 (2010). https://doi.org/10.1063/1.3391670

40 Bellunato, A. & Schneider, G. F. Electrophilic Radical Coupling at the Edge of Graphene. *Nanoscale* **10**, 12011-12017 (2018). https://doi.org/10.1039/C8NR03429J

41 Xia, Z. *et al.* Electrochemical Functionalization of Graphene at the Nanoscale with Self-assembling Diazonium Salts. *ACS Nano* **10**, 7125-7134 (2016). https://doi.org/10.1021/acsnano.6b03278

42 Rodríguez, S. J., Makinistian, L. & Albanesi, E. A. Graphene for Amino Acid Biosensing: Theoretical Study of the Electronic Transport. *Applied Surface Science* **419**, 540-545 (2017). https://doi.org/https://doi.org/10.1016/j.apsusc.2017.05.031

43 Malard, L. M. *et al*. Raman Spectroscopy in Graphene. *Physics Reports* **473**, 51-87 (2009). https://doi.org/https://doi.org/10.1016/j.physrep.2009.02.003

44 Ferrari, A. C. & Basko, D. M. Raman Spectroscopy as a Versatile Tool for Studying the Properties of Graphene. *Nature Nanotechnology* **8**, 235-246 (2013). https://doi.org/10.1038/nnano.2013.46

45 Greenwood, J. *et al.* Covalent Modification of Graphene and Graphite Using Diazonium Chemistry: Tunable Grafting and Nanomanipulation. *ACS Nano* **9**, 5520-5535 (2015). https://doi.org/10.1021/acsnano.5b01580

46 Hirschorn, B. *et al.* Determination of Effective Capacitance and Film Thickness from Constant-phase-element Parameters. *Electrochimica Acta* **55**, 6218-6227 (2010). https://doi.org/https://doi.org/10.1016/j.electacta.2009.10.065

47 Xia, J. *et al*. Measurement of the Quantum Capacitance of Graphene. *Nature Nanotechnology* **4**, 505-509 (2009). https://doi.org/10.1038/nnano.2009.177

48 Wetzl, C. *et al.* Covalent Functionalisation Controlled by Molecular Design for the Aptameric Recognition of Serotonin in Graphene-based Field-effect Transistors. *Nanoscale* **15**, 16650-16657 (2023). https://doi.org/10.1039/D3NR04153K

49 Rodrigues, T. *et al.* Highly Performing Graphene-based Field Effect Transistor for the Differentiation Between Mild-moderate-severe Myocardial Injury. *Nano Today* **43**, 101391 (2022). https://doi.org/https://doi.org/10.1016/j.nantod.2022.101391

50 Piccinini, E. *et al.* Surface Engineering of Graphene through Heterobifunctional Supramolecular-Covalent Scaffolds for Rapid COVID-19 Biomarker Detection. *ACS Applied Materials & Interfaces* **13**, 43696-43707 (2021). https://doi.org/10.1021/acsami.1c12142

51 Ksiazek, T. G. *et al*. ELISA for the Detection of Antibodies to Ebola Viruses. *The Journal of Infectious Diseases* **179**, S192-S198 (1999). https://doi.org/10.1086/514313

52 Rissin, D. M. *et al.* Single-molecule Enzyme-linked Immunosorbent Assay Detects Serum Proteins at Subfemtomolar Concentrations. *Nature Biotechnology* **28**, 595-599 (2010). https://doi.org/10.1038/nbt.1641

53 Huang, A. *et al*. Quantitative Fluorescence Quenching on Antibody-conjugated Graphene Oxide as a Platform for Protein Sensing. *Scientific Reports* **7**, 40772 (2017). https://doi.org/10.1038/srep40772

54 Gómez-Santos, G. & Stauber, T. Fluorescence Quenching in Graphene: A Fundamental Ruler and Evidence for Transverse Plasmons. *Physical Review B* **84**, 165438 (2011). https://doi.org/10.1103/PhysRevB.84.165438

55 Klimeš, J. *et al*. Chemical Accuracy for the Van der Waals Density Functional. *Journal of Physics: Condensed Matter* **22**, 022201 (2010). https://doi.org/10.1088/0953-8984/22/2/022201

56 Klimeš, J. *et al*. Van der Waals Density Functionals Applied to Solids. *Physical Review B* **83**, 195131 (2011). https://doi.org/10.1103/PhysRevB.83.195131

57 Klimeš, J., Bowler, D. R. & Michaelides, A. Van der Waals Density Functionals Applied to Solids. *Physical Review B* **83**, 195131 (2011). https://doi.org/10.1103/PhysRevB.83.195131

58 Klimes, J. *et al*. Chemical Accuracy for the Van der Waals Density Functional. *Journal of Physics: Condensed Matter* **22**, 022201 (2010). https://doi.org/10.1088/0953-8984/22/2/022201

59 Pak, A. J., Paek, E. & Hwang, G. S. Impact of Graphene Edges on Enhancing the Performance of Electrochemical Double Layer Capacitors. *The Journal of Physical Chemistry C* **118**, 21770-21777 (2014). https://doi.org/10.1021/jp504458z

60 Pak, A. J., Paek, E. & Hwang, G. S. Impact of Graphene Edges on Enhancing the Performance of Electrochemical Double Layer Capacitors. *The Journal of Physical Chemistry C* **118**, 21770-21777 (2014). https://doi.org/10.1021/jp504458z

61 Zhan, C. *et al*. Quantum Effects on the Capacitance of Graphene-Based Electrodes. *The Journal of Physical Chemistry C* **119**, 22297-22303 (2015). https://doi.org/10.1021/acs.jpcc.5b05930

62 Ghahghaei, Z. *et al*. Removing Phenol Contaminants from Wastewater using Graphene Nanobuds: DFT and Reactive MD Simulation Investigations. *Journal of Molecular Liquids* **286**, 110872 (2019). https://doi.org/https://doi.org/10.1016/j.molliq.2019.04.149

4.6 Supporting information

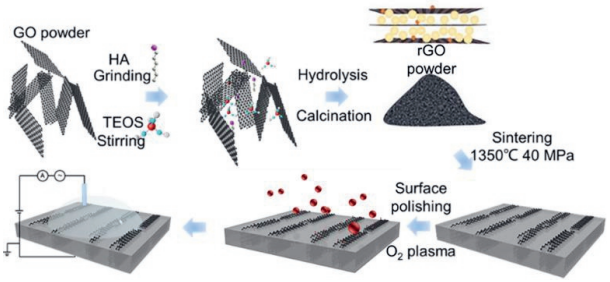

Figure S1. Schematic illustration of the preparation process for rGO/SiO_2 ceramic composites. The fabrication of the eGQC sensor with exposed graphene edges involved embedding parallel rGO sheets within a SiO_2 matrix through a previously established intercalation and pressure sintering approach. Hexylamine (HA) molecules were first used to expand the interlayer spacing of graphene oxide (GO), followed by co-intercalation with tetraethyl orthosilicate (TEOS), a SiO_2 precursor. The disordered GO/SiO_2 powder was subsequently reduced and consolidated into dense ceramic composites containing 6 vol% rGO via pressure sintering.

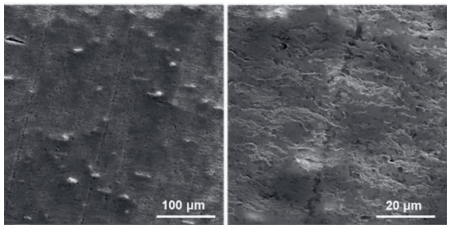

Figure S2. SEM image of graphene edge matrix. After vertical sectioning of the parallel-aligned rGO sheets, followed by mechanical polishing, smooth surfaces were achieved, characterized by a high density of perpendicular rGO edges tightly embedded within the ceramic matrix.

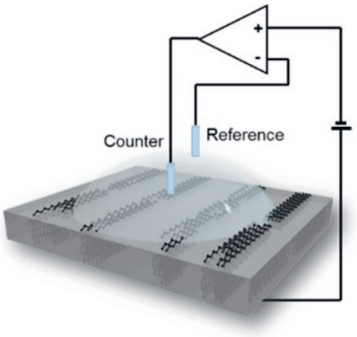

Figure S3. Schematic diagram of electrochemical functionalization of NHS-Ph-N_2^+. Aryl radicals were electro-grafted from NHS-Ph-N_2^+ via nitrogen cleavage, generating electrophilic NHS-aryl radicals that readily react with the nucleophilic graphene edges. The application of a potential difference between the

graphene edge and the counter electrode not only drives the electrophilic reactions but also enhances the electronic density of states at the graphene edge. This facilitates orbital overlap between the highest occupied molecular orbital (HOMO) of the graphene edge and the lowest unoccupied molecular orbital (LUMO) of the aryl radicals, promoting covalent bonding to carbon atoms as well as hydroxyl or carboxyl groups present at the graphene edge.

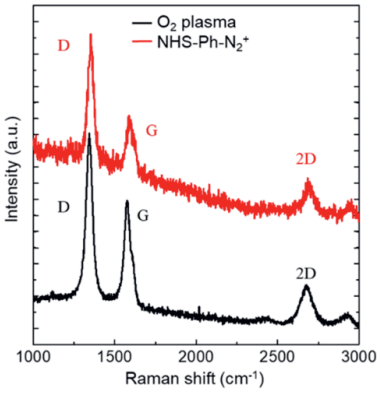

Figure S4. Raman spectrum before and after NHS-Ph-N_2^+ treatment. The diazonium salt reaction induces a transformation of carbon atoms at the graphene edge from sp^2 to sp^3 hybridization, leading to notable structural changes. This transition disrupts the conjugated π-electron system of the graphene edge, thereby modifying its electronic and vibrational properties. As a result, the Raman intensity ratio I_D/I_G exhibits a pronounced increase.

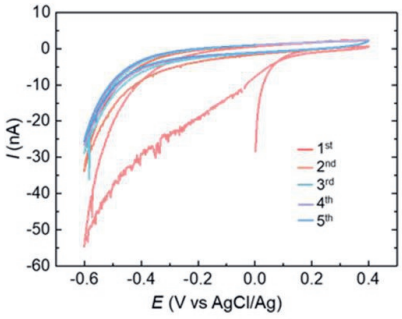

Figure S5. Graphene edge with NHS-Ph-N_2^+ by electrochemistry. The reduction in current density at negative oxidative potentials observed during cyclic voltammetry (CV), particularly between the first and subsequent cycles, provides compelling evidence for the formation of a functional passivation layer on the graphene edge. This passivation layer exhibits chemical properties comparable to those reported for the electrografting of nitrobenzene onto graphene surfaces. Specifically, the NHS moieties derived from NHS-Ph-N_2^+ establish an insulating layer that effectively passivates the graphene electrode, preventing further radical binding. This phenomenon is further validated by the stabilization of the CV

curves after the initial three cycles.

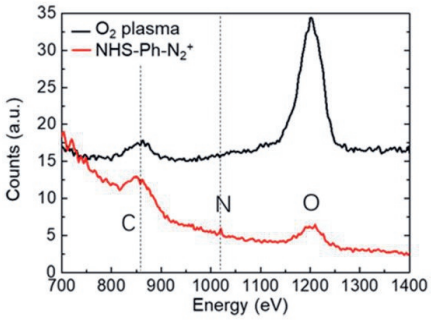

Figure S6. The LIES spectrum of graphene edge before and after NHS-Ph-N_2^+ functionalization. Low-energy ion scattering (LEIS) was utilized to analyze the elemental distribution on graphene edge samples. The LEIS spectra displayed the anticipated features, confirming the presence of nitrogen (N) and carbon (C) elements. Specifically, a nitrogen signal was detected at 1027 eV, while a carbon signal was observed at 848 eV. These findings provide compelling evidence for the successful incorporation of nitrogen species at the graphene edges, likely resulting from functionalization processes.

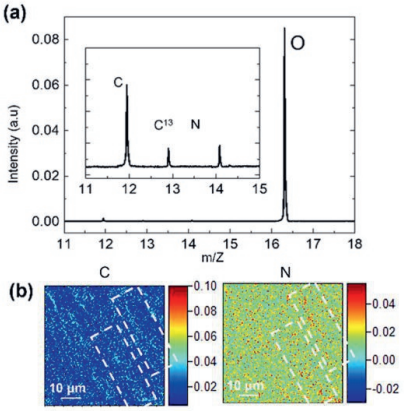

Figure S7. The TOF-SIMS spectrum and mapping. **(a)** The TOF-SIMS spectrum of graphene edge after NHS-Ph-N_2^+ functionalization. **(b)** Maps of the spatial distribution of C and N elements after NHS-Ph-N_2^+ functionalization. Following the electrochemical grafting of diazonium salts, nitrogen (N) originating from the diazonium compounds was unambiguously detected, displaying a spatial distribution closely aligned with that of carbon (C). This alignment confirms the successful covalent functionalization of the graphene edges. The uniform co-localization of N and C elements provides robust evidence of an efficient and well-controlled grafting process. Moreover, the stability and reproducibility of this functionalization were validated through successive regeneration cycles, during which the N distribution consistently mirrored that of the C atoms. These results underscore the robustness of the diazonium grafting strategy, yielding functionalized graphene surfaces with high stability and reproducibility.

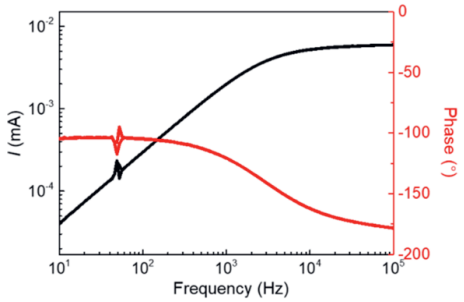

Figure S8. Frequency-dependent current amplitude and phase of eGQC biosensor measured in a 0.01×PBS solution. To optimize measurement accuracy, a careful balance was struck between the trade-offs associated with electrical noise at lower frequencies and reduced precision at higher frequencies due to the decreasing capacitive reactance. Consequently, the bias-dependent interfacial capacitance was monitored at an intermediate frequency of 172 Hz. At this frequency, the capacitive impedance is dominant, ensuring reliable and robust data acquisition.

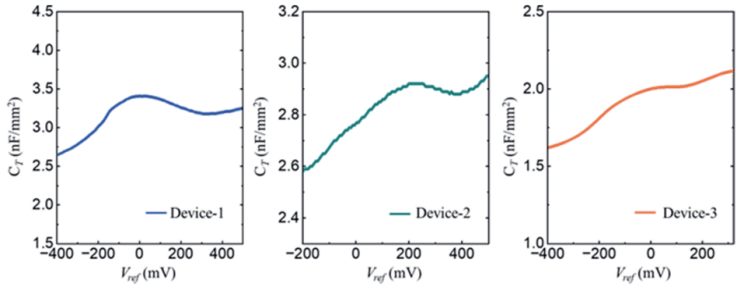

Figure S9. Total effective interfacial capacitance (C_T) of the different eGQC chip plotted against reference voltage (V_{ref}).

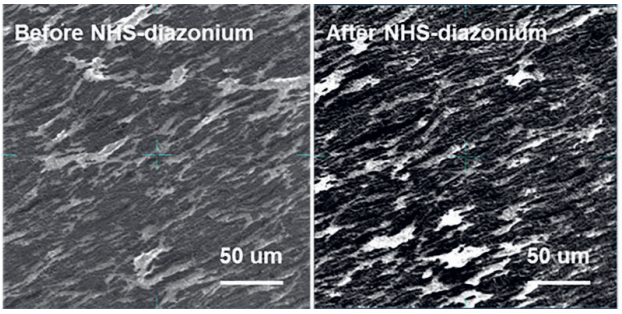

Figure S10. SEM image of graphene edge matrix before and after NHS-diazonium functionalization.

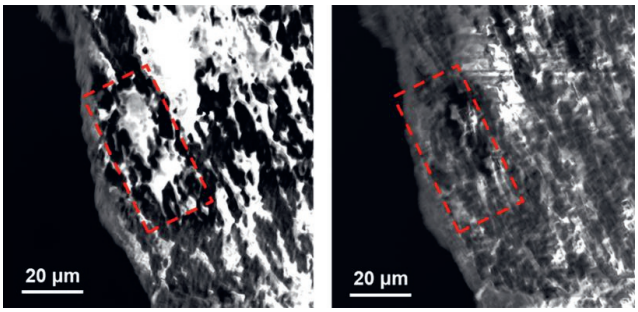

Figure S11. DNA complex on the surface of graphene edge device before and after O_2 plasma etching. We deposited 10 μL of a 10 μM DNA solution onto the sensor surface. To facilitate SEM observation, the DNA solution was allowed to air-dry, followed by immersion in deionized water. This process induced excessive aggregation of DNA polymers on the sensor surface. Subsequent oxygen plasma treatment effectively removed the DNA molecules, leaving a relatively clean surface.

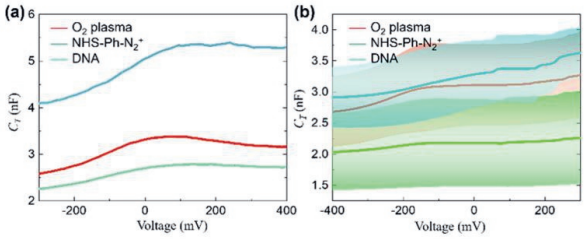

Figure S12. The edge quantum capacitance response under different functionalization stage. **(a)** Capacitance of graphene edge under different functionalization processes. **(b)** Capacitance of graphene edge under different functionalization processes in 100 times. The edge quantum capacitance response was recorded at each of the three stages: after edge preparation, NHS-Ph-N_2^+ functionalization, and DNA incubation. We regenerate the biosensor by using O_2 plasma to remove the biopolymer coupled at the edge of graphene. The same process was repeated for 100 times for the same device and the capacitance profile of the functionalization process were recorded at each 6 intervals.

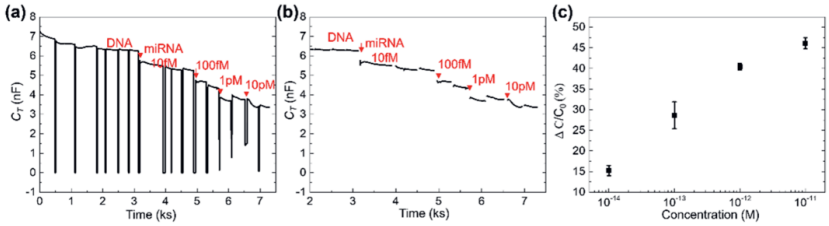

Figure S13. Data processing for the signals obtained from the miRNA sensing experiments **(a)** The C_T-t curve under changing miRNA concentrations. **(b)** The C_T-t curves under varying miRNA concentrations after removal of solution-change-induced spikes. Spikes caused by solution changes were excluded from the data analysis. **(c)** The changes of current as a function of miRNA concentrations. As the target miRNA concentration increases to 10fM, 100 fM, 1 pM, and 10 pM, the capacitance gradually decreases due to the doping effect induced by charge accumulation. Notably, the capacitance response exhibits a more

pronounced change at low concentrations (10 fM), highlighting the sensor's sensitivity in detecting minimal target levels. At higher concentrations, the response amplitude diminishes, likely due to the saturation of binding sites. The device demonstrates an exceptional limit of detection, reaching as low as 10 fM. The observed spikes correspond to current fluctuations caused by the solution change. Assuming a linear response at low concentrations, the limit of detection (LOD) can be estimated to be 147 aM, corresponding to a signal-to-noise ratio (SNR) of 3.

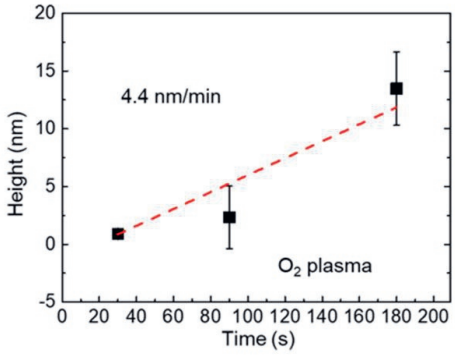

Figure S14. O_2 plasma etching rate estimation. A multilayer graphene sheet with an initial thickness of approximately 300 nm was prepared via mechanical exfoliation. Following the initial thickness measurement, the graphene was subjected to oxygen plasma treatment at 120 W for 30 s, 90 s, and 180 s. The thickness of the graphene was subsequently measured using atomic force microscopy (AFM). This approach enabled us to determine the etching rate of graphene under oxygen plasma conditions.

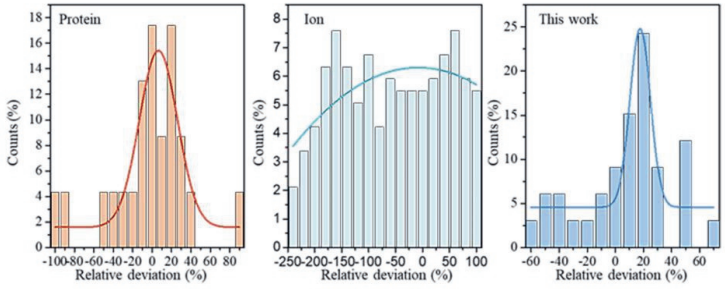

Figure S15. Statistic diagram of device variations of resuable graphene edge device and the state-of-art Gr-FET arrays. Gr-FET array shows relative large fluctuations across different devices. In contrast, our covalently functionalized eGQC chip yields favorably device variations of 18 ± 1.9 %.

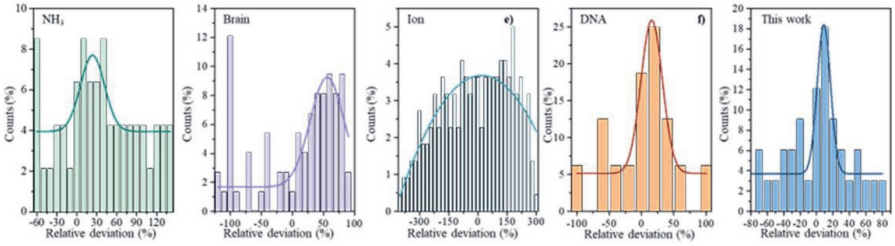

Figure S16. Statistic diagram of device variations of resuable graphene edge device and the state-of-art Gr-FET arrays. The Gr-FET array shows significant fluctuations across different devices (Gr-FET arrays NH_3 gas sensor, brain activity sensor, ion sensor and DNA sensor are 24 ± 6.5%, 56 ± 4.4% , 18 ± 19% , 16 ± 3.8%, respectively). In contrast, our covalently functionalized eGQC chip yields favorably sensing variations of 8.9 ± 1.7%.

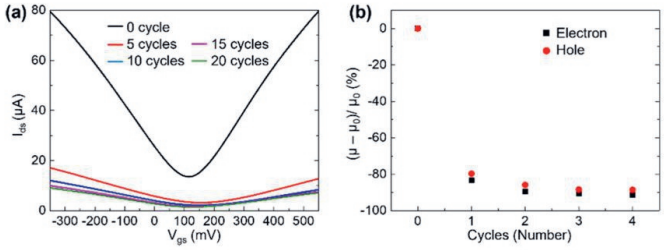

Figure S17. Changes in electrical properties of Gr-FET after NHS-Ph-N_2^+electrochemical functionalization of graphene surface **(a)** Transfer characteristic curve of Gr-FET after NHS-diazonium salt covalent modification of graphene surface. **(b)** Changes in Gr-FET carrier mobility after NHS-diazonium salt covalent modification of graphene surface. The I_{ds}-V_{gs} transfer characteristics of the GrFET were measured using a Keithley instrument. For the transfer characteristic measurements, the V_{gs} was swept from -350 mV to 550 mV at a V_{ds} of 100 mV. The transfer characteristic curves of the Gr-FET, recorded under different durations of diazonium salt and graphene electrochemical functionalization. The changes in Gr-FET mobility corresponding to the number of electrochemical cycles are extracted. As diazonium electrochemical grafting occurs on the graphene surface, an increasing number of carbon atoms undergo a transition from sp^2 to sp^3 hybridization, leading to a rapid decrease in the device mobility by approximately 90%.

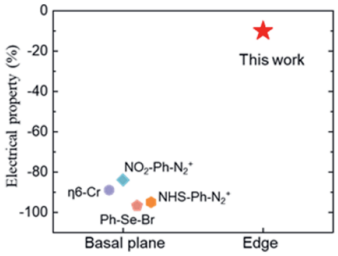

Figure S18. Statistic diagram of electrical performance decrease variations of resuable graphene edge device and the state-of-art covalent functionalization Gr-FET sensor. The Gr-FET sensor shows electrical performance (current or mobility) decreases by at least 80% after covalent functionalization. In contrast, the covalent functionalization of the eGQC-Chip results in minimal impact on the quantum capacitance performance, with a change of less than 10%.

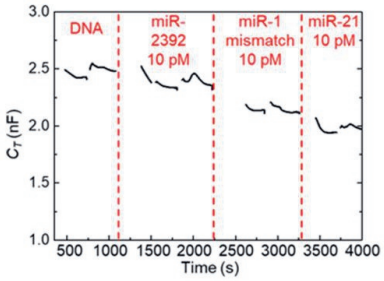

Figure S19. Selectivity of graphene edge device with non-complementary RNA (miR-2392), single base mismatched RNA (miR-1 mismatch) and fully complementary RNA (miR-21). Our results revealed minimal capacitance response when employing completely non-complementary RNA sequences.

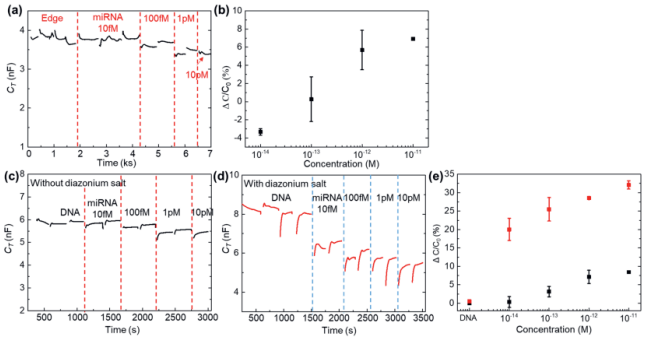

Figure S20. (a) Capacitance changes as a function of miRNA concentrations after passivated with Tween-20. **(b)** Sensing response of graphene edges passivated with Tween-20. **(c)** Sensing test of graphene edge unfunctionalized diazonium salt (black) and **(d)** functionalized diazonium salt linker (red). **(e)** The signal response of unfunctionalized edge and diazonium functionalized edge. Weak signal response caused by non-specific adsorption of RNA on graphene edges.

Tween-20 passivation effectively reduces non-specific adsorption, as evidenced by the negligible sensing response. This highlights the role of Tween-20 in enhancing sensor specificity by minimizing background interference, ensuring selective detection of target molecules. After confirming the passivation effectiveness of Tween-20, the performance of diazonium functionalization was further evaluated. The sensing response of untreated graphene edges to miRNA is relatively low (<10%), while the diazonium-functionalized sensor shows a significant enhancement in response, exceeding 30%, particularly at low miRNA concentrations. This notable increase underscores the importance of covalent diazonium salt functionalization for effective immobilization of complementary DNA probes.

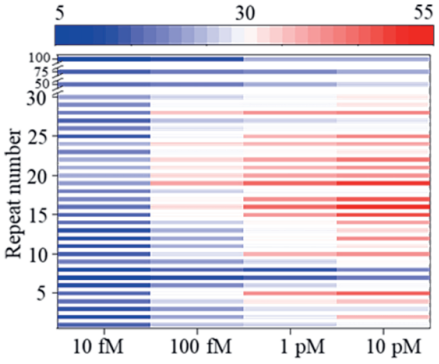

Figure S21. The heat map of capacitance responses across 100 repeated tests. In the heat map illustrating capacitance responses across 100 repeated tests, the color gradient transitioning from blue to red signifies increasing capacitance response values. Notably, distinct color variations are observed corresponding to different miRNA concentrations. As the miRNA concentration increases, the colors deepen progressively, highlighting a clear and consistent response to varying miRNA levels. This trend remains evident even after 100 repeated tests, underscoring the high sensitivity and reliability of the device in detecting and distinguishing miRNA concentrations.

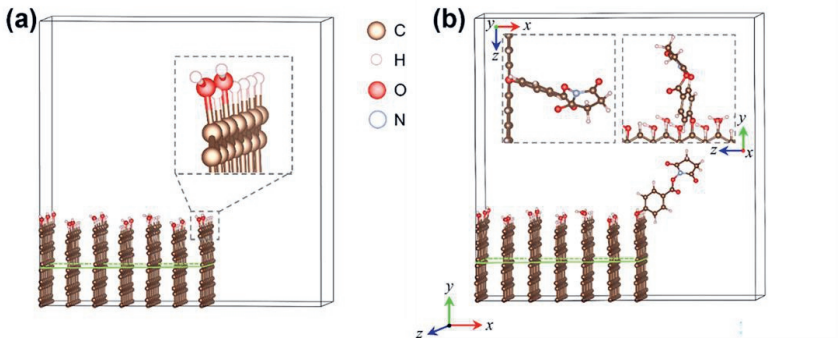

Figure S22. Optimized graphene models **(a)** terminated with hydroxyl groups and hydrogen atoms (inset: the enlarged view of terminated hydroxyl groups) and **(b)** functionalized via NHS-diazonium salt (inset: the enlarged top and side views of covalent functionalization).

Synthesis of NHS diazonium salt (similar as in Chapter 2).

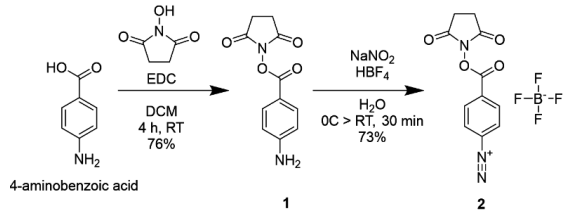

Figure S23. Synthetic route to compounds **1** and **2**. Compound **1** was prepared via EDC/NHS-mediated activation of 4-aminobenzoic acid to afford the corresponding N-Hydroxy succinimide ester in 76% yield. Subsequent diazotization of **1** with $NaNO_2$_22 in the presence of HBF4_44 at low temperature yielded the corresponding aryl diazonium tetrafluoroborate **2** in 73% yield. The structures of both intermediates were confirmed by NMR spectroscopy and ESI-MS.

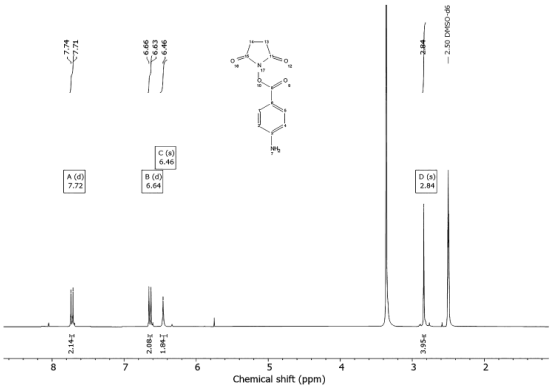

Figure S24. ^{1}H NMR of **1** in DMSO-d_6. The red labels A–E denote the ^{1}H signals corresponding to the diazonium salt.

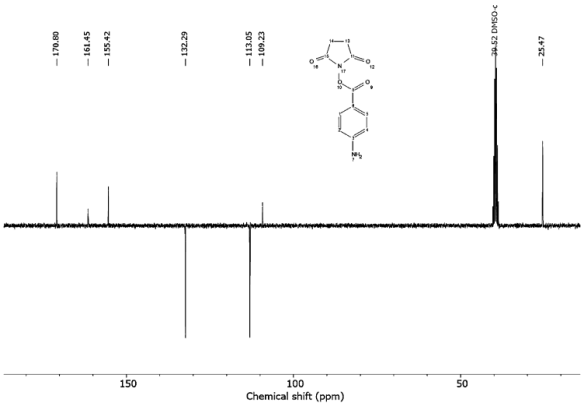

Figure S25. ^{13}C NMR of **1** in DMSO-d_6.

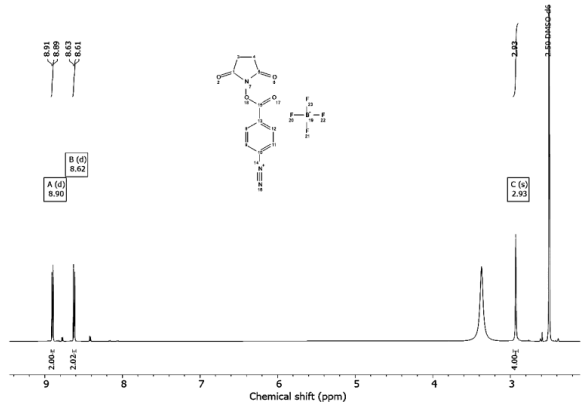

Figure S26. ^{1}H NMR of **2** in DMSO-d_6.

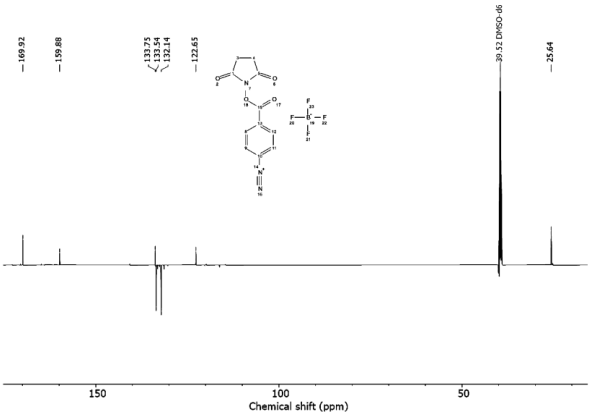

Figure S27. ^{13}C NMR of **2** in DMSO-d_6.

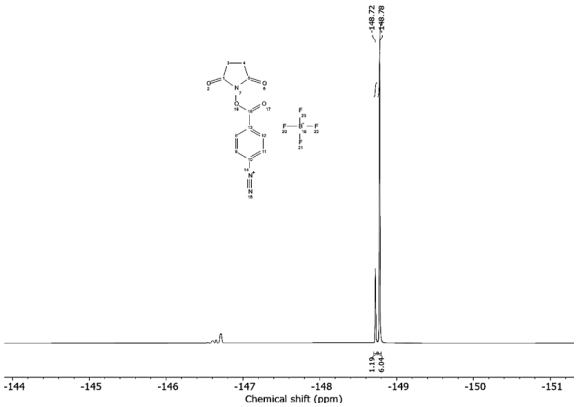

Figure S28. ^{19}F NMR of **2** in DMSO-d_6. Two closely spaced signals at δ −148.72 and −148.78 ppm are observed for the tetrafluoroborate counterion.

Functionalization	Target	Detection limitation
NHS-Ph-N_2^+	Serotonin	1 μM
Vinylsulfonated-polyamines	Concanavalin A	2.5 nM
TIPS-Eth-ArN_2^+	Protein	10 pg/mL
N-Heterocyclic Carbene	Antibody	1 pg/mL
Our work	miRNA	**10 fM**

Table S1. Comparison of detection limits of current graphene covalent functionalized biosensor, including NHS-Ph-N_2^+, vinylsulfonated-polyamines (PA-VS), TIPS-Eth-ArN_2^+, N-Heterocyclic Carbene (NHC).